

Comprehensive thermal modelling and characterization of an electro-thermal-compliant microactuator

Nilesh D Mankame and G K Ananthasuresh¹

Department of Mechanical Engineering and Applied Mechanics, University of Pennsylvania, 297 Towne Building, 220 South 33rd Street, Philadelphia, PA 19104, USA

E-mail: nileshdm@seas.upenn.edu and gksuresh@seas.upenn.edu

Received 4 October 2000, in final form 28 February 2001

Published 19 July 2001

Online at stacks.iop.org/JMM/11/452

Abstract

A comprehensive thermal model for an electro-thermal-compliant (ETC) microactuator is presented in this paper. The model accounts for all modes of heat dissipation and the temperature dependence of thermophysical and heat transfer properties. The thermal modelling technique underlying the microactuator model is general and can be used for the virtual testing of any ETC device over a wide range of temperatures (300–1500 K). The influence of physical size and thermal boundary conditions at the anchors, where the device is connected to the substrate, on the behaviour of an ETC microactuator is studied by finite element simulations based on the comprehensive thermal model. Simulations show that the performance ratio of the microactuator increased by two orders of magnitude when the characteristic length of the device was increased by one order of magnitude from 0.22 to 2.2 mm. Restricting heat loss to the substrate via the device anchors increased the actuator stroke by 66% and its energy efficiency by 400%, on average, over the temperature range of 300–1500 K. An important observation made is that the size of the device and thermal boundary conditions at the device anchor primarily control the stroke, operating temperature and performance ratio of the microactuator for a given electrical conductivity.

(Some figures in this article are in colour only in the electronic version)

1. Introduction

Compact and energy efficient microactuators that yield high output force and displacement find uses in microsystems applications ranging from telecommunications to medicine. Thermal microactuators are compact and can provide high output force. Bimorph-like thermal actuators are composite structures made of two or more layers of materials with differing coefficients of linear thermal expansion (see, for example, [1]). A different category of thermal actuators comprises single material structures whose behaviour is controlled largely by the topology and shape of the structure. Electro-thermally actuated compliant (ETC) microactuators, which are the focus of this paper, belong to the latter category. The application of a voltage difference between two or

more points of an arbitrary, electrically conducting, elastic continuum produces Joule heating. The topology and shape of the continuum give rise to non-uniform Joule heating and hence non-uniform thermal expansion. Moreover, the topology and shape of the continuum direct this constrained thermal expansion to effect an elastic deformation of a magnitude greater than that obtained by uniform heating. This is the principle of operation of a generic ETC device [2]. An elegant example of an ETC microactuator is the Guckel actuator [3] for in-plane motion shown in figure 1. The Guckel microactuator will be referred to as ‘the microactuator’ or ‘the basic ETC microactuator’ in the rest of the paper for brevity. The thin arm of the microactuator has a higher electrical resistance than the wide arm. The thin arm therefore gets heated more than the wide arm and consequently elongates more than the wide arm. The greater compliance of the microactuator structure in the bending mode as compared to axial elongation mode then

¹ Author to whom correspondence should be addressed.

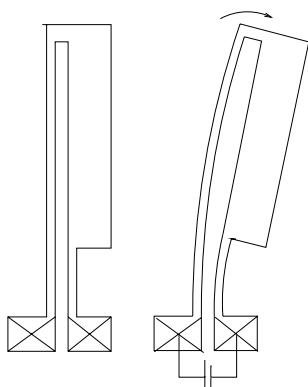


Figure 1. The Guckel ETC microactuator in its original (left) and deflected configurations (right).

results in an amplification of the relatively small difference in axial thermal expansions of the two arms of the structure into a large lateral motion as seen in figure 1.

ETC microactuators yield a higher output force ($O(1 \text{ mN})$) at a significantly lower drive voltage (5–10 V) than electrostatic actuators of comparable size, which have output forces of $O(1 \mu\text{N})$ at drive voltages of 100 V [4]. ETC actuators are also easy to fabricate because of their unitized construction and are compatible with both the manufacturing processes as well as the voltage–current operation regime of CMOS microelectronics [5]. These microactuators have therefore attracted a lot of attention in recent years [2, 6–8]. Comtois and co-workers [5, 9] have characterized the steady-state and dynamic performance of the microactuator and proposed guidelines for its design. Lerch *et al* [10] have reported on a finite element (FE) analysis of a gripper based on the microactuator for a maximum temperature in the device of approximately 800 K. The FE simulations yielded a temperature distribution that agreed to within 10% of the temperature distribution obtained from IR photo-thermometry. Lin and Chiao [11] have used FE simulations to study the electrothermal response of lineshape microstructures. Jonsmann *et al* [12] have introduced FE simulation-based topology optimization as a tool for systematic design of planar ETC microactuators. Moulton and Ananthasuresh [2] have used FE simulations to demonstrate a building-block approach to the synthesis of general ETC devices.

The behaviour of an ETC device is governed by a coupled nonlinear electro-thermal-elastic boundary value problem. The formulation of the boundary value problem for a homogeneous, material isotropic in all three energy domains is summarized in table 1. The resistive heating and temperature dependence of thermophysical properties couple the electrical and thermal problems. The temperature dependence of thermophysical properties and radiative heat transfer make the problem highly nonlinear.

Surface heat transfer by convection and radiation (which contribute to f_{nT}) becomes important at high operating temperatures (above 500 K) and also at small physical device sizes. The nature of thermal boundary conditions at the device anchor also significantly influences the behaviour of an ETC device. These two aspects of thermal modelling of the microactuator are elaborated in section 2. Intra-device radiation heat exchange in ETC devices occurs between parts

of the device that can ‘see’ each other. This mode of heat transfer is especially important in devices such as the basic ETC microactuator, which have closely spaced parts with a high temperature difference between them. Polder and Hove [13] have observed that heat exchange between two narrowly spaced bodies increases strongly with decreasing inter-body spacing in the range of 1–10 μm . Conductive heat transfer from the bottom surface of the device to the substrate through the intervening air film becomes an important component of surface heat transfer (f_{nT}) when the air film is very thin. Lin and Chiao [11] have used numerical simulations to obtain an empirical shape factor that accounted for this mode of heat transfer in plate-like microstructures suspended over a substrate by a thin (2 μm) air film.

ETC devices are known to operate over a wide temperature range (300–1500 K) [14, 15]. For non-degenerately doped semiconductors such as silicon, the thermophysical properties such as thermal and electrical conductivities [16, 17], thermoelastic properties such as Young’s modulus [18] and the coefficient of linear thermal expansion [19] and heat transfer properties such as convective film coefficients are strongly dependent on the temperature [20]. It is, therefore, necessary to consider the nonlinearities introduced by temperature-dependent properties and radiative heat exchange, when the behaviour of an ETC device is to be accurately modelled over a wide temperature range.

Okada and Tokumaru [19] have shown that the coefficient of linear thermal expansion, α , for single-crystal silicon, varies by more than 60% over the temperature range of 300–1500 K. Ono *et al* [18] reported a sharp 20% fall in the value of the Young’s modulus E between 1073 and 1273 K in their study of the temperature dependence of E for single-crystal silicon in the 290–1273 K range. Mills [21] has summarized natural convection correlations for different configurations and geometries. The film heat transfer coefficients for natural convection increase with increasing temperature and diminishing size. Lide and Kehiaian [16] have given a 130% fall in the thermal conductivity, k_t , of single-crystal silicon when the temperature was increased from 300 to 1000 K. Both the magnitude as well as the nature of temperature dependence of electrical conductivity (k_e) for semiconductors can be varied significantly by the process of doping. A set of k_e versus T and k_t versus T that is physically inconsistent would lead to unbounded temperature rise and/or spurious results. Since, thermal conductivity is not strongly dependent on the doping level [17], the determination of the temperature dependence of electrical conductivity for a given doping level is crucial for accurate modelling of the device behaviour over a wide temperature range.

The above discussion motivates the following requirements of a comprehensive thermal model, for a generic ETC device that is accurate over a wide temperature range:

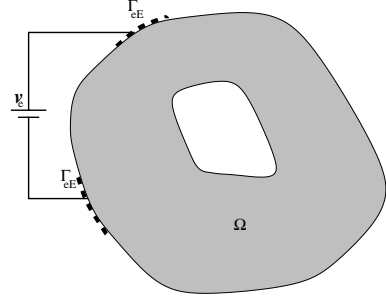
- nonlinearity introduced by the temperature dependence of thermophysical and heat transfer properties must be accounted for in the model;
- surface heat loss by radiation and convection, intra-device heat transfer and heat loss to the substrate by conduction through trapped air volumes must be modelled;
- the appropriate thermal boundary condition at the device anchors must be modelled.

Table 1. The set of boundary value problems governing the behaviour of an ETC device.

Electrical boundary value problem

$$\begin{aligned} \nabla \cdot (k_e \nabla v(\mathbf{r})) &= 0 && \text{in } \Omega \\ v &= v_e && \text{on } \Gamma_{eE} \end{aligned}$$

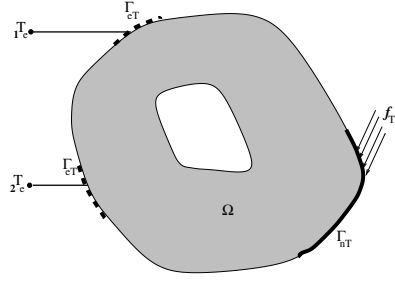
where v is the electrical potential, \mathbf{r} is the position vector, $k_e(T, \mathcal{D})$ is the temperature and doping level dependent electrical conductivity and v_e is the imposed voltage.



Thermal boundary value problem

$$\begin{aligned} \nabla \cdot (k_t \nabla T(\mathbf{r})) + \dot{q}_t &= 0 && \text{in } \Omega \\ \dot{q}_t &= k_e \nabla v \cdot \nabla v && \text{in } \Omega \\ T &= T_e && \text{on } \Gamma_{eT} \\ \mathbf{n}(\mathbf{r}) \cdot (k_t \nabla T(\mathbf{r})) &= f_{nT} && \text{on } \Gamma_{nT} \end{aligned}$$

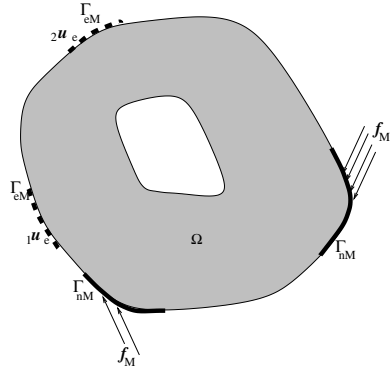
where T is the temperature, $k_t(T)$ is the temperature-dependent thermal conductivity, \dot{q}_t is the volumetric heat generation rate, T_e is the imposed temperature, \mathbf{n} is the unit normal to the surface and $f_{nT}(T)$ is the temperature-dependent boundary heat flux. Radiation and convection or conduction, in some cases, contribute to f_{nT} .



Elastic boundary value problem

$$\begin{aligned} \nabla \cdot \tilde{\boldsymbol{\sigma}}(\mathbf{r}) + \mathbf{F}(\mathbf{r}) &= 0 && \text{in } \Omega \\ \tilde{\boldsymbol{\sigma}} &= \mathbf{E}(\tilde{\boldsymbol{\epsilon}} - \alpha(T - T_0)\tilde{\mathbf{I}}) && \text{in } \Omega \\ \tilde{\boldsymbol{\epsilon}} &= \frac{[\nabla \mathbf{u}(\mathbf{r}) + (\nabla \mathbf{u}(\mathbf{r}))^T]}{2} && \text{in } \Omega \\ \mathbf{u} &= \mathbf{u}_e && \text{on } \Gamma_{eM} \\ \tilde{\boldsymbol{\sigma}} \mathbf{n} &= \mathbf{f}_M && \text{on } \Gamma_{nM} \end{aligned}$$

where $\tilde{\boldsymbol{\sigma}}$, $\tilde{\boldsymbol{\epsilon}}$, $\tilde{\mathbf{I}}$ and $\mathbf{E}(T)$ are the stress, strain, identity and temperature-dependent elasticity tensors, $\alpha(T)$ is the temperature-dependent linear coefficient of thermal expansion, T_0 is initial temperature, \mathbf{u} is the displacement field, \mathbf{u}_e is the imposed displacement, \mathbf{F} is the body force and \mathbf{f}_M is the surface traction.



It is also desirable that the model be *device independent* so that standard property databases can be used to eliminate device-specific empirical correction factors.

Past efforts at modelling thermal devices at small length scales [2, 8, 10–12, 22] did not consider heat loss by radiation or the temperature dependence of thermophysical and heat transfer properties for the device. The thermal models presented in the above references are, therefore, either restricted to small temperature excursions (300–800 K) or are specific to the configuration being modelled.

This paper presents a comprehensive thermal model for the steady-state analysis of the basic ETC microactuator. The model includes surface heat transfer via radiation, convection and conduction, the effect of thermal boundary conditions at the device anchors, the temperature dependence of thermophysical properties and the physical size dependence of surface heat transfer properties. Although the modelling results presented in this paper are in the context of a particular ETC device, the method is general and can be used for the simulation and analysis of a generic ETC device at different physical sizes and over a wide range of maximum

operating temperature for the device. A finite element implementation of the model in ABAQUS® [23], a commercial FE analysis package, is validated by comparing its results with experimental data. The *no-load operating characteristics* for the microactuator at two different physical sizes and under two different thermal boundary conditions are obtained from the simulations. The characteristics serve to guide the selection of thermal boundary conditions and physical size of the device while designing the microactuator.

2. Thermal boundary conditions for an ETC device

This section addresses two aspects of thermal modelling that have not been considered in previous research on microscale devices.

2.1. Convective and radiative heat transfer

At steady state, an ETC device dissipates the entire amount of electrical power in the form of heat to maintain the steady-state temperature profile. At low temperatures (less than 500 K),

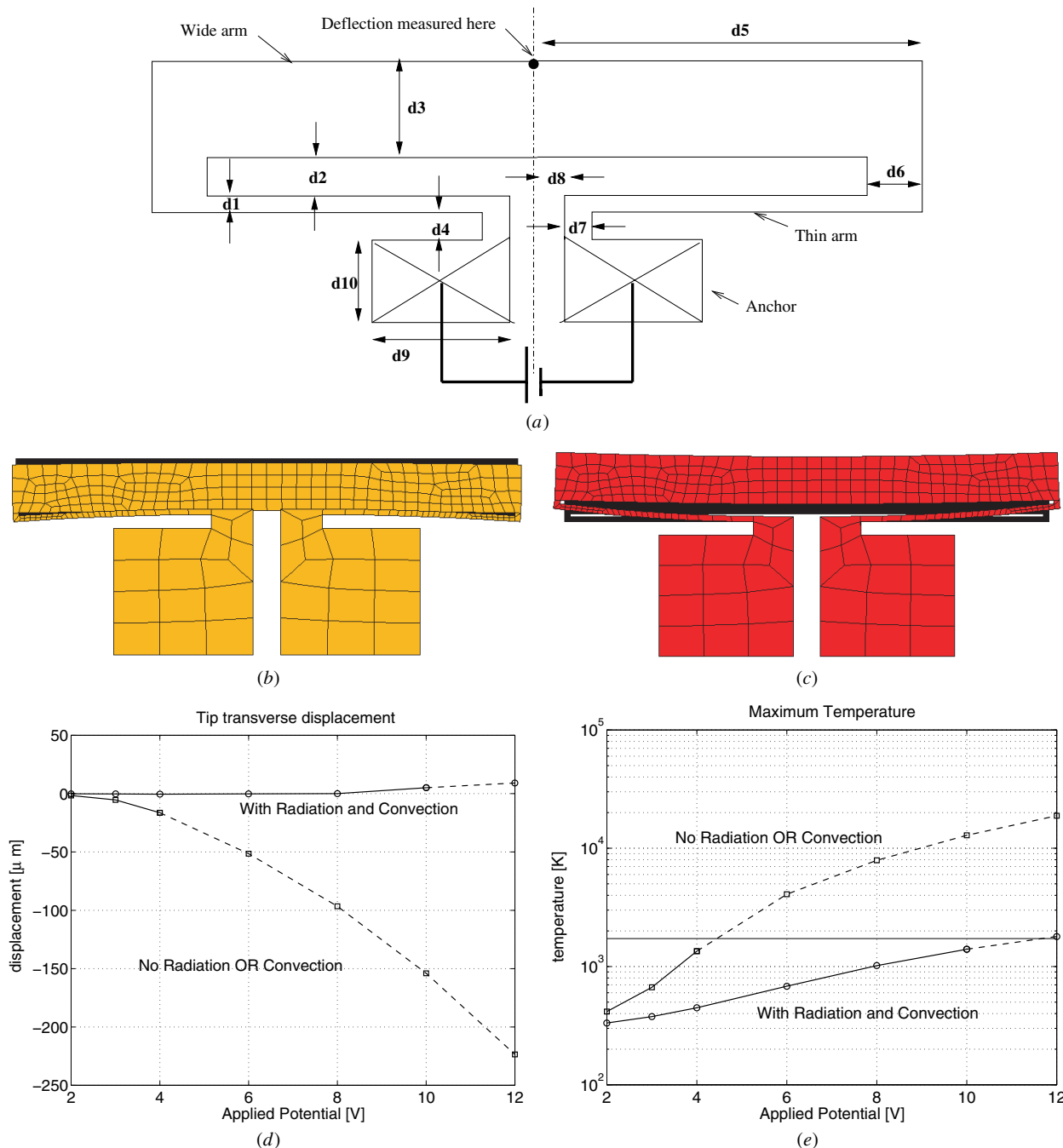


Figure 2. (a) Schematic diagram of TED. (b) Deflected profile for single meso scale EBC device modelled without convection or radiation and (c) with convection and radiation. (d) Transverse displacement of TED with and without convection and radiation. The dashed line corresponds to when the maximum temperature in the device is more than 1750 K—the melting point of single-crystal silicon. (e) Maximum temperature in the TED with and without convection and radiation.

the heat generated within the device is largely conducted to the ground via the device anchors [24]. However, at high operating temperatures (above 500 K) radiation and convection heat transfer modes become significant. This is especially true as the device size reduces because the ratio of surface area to volume of a solid increases with diminishing size. Some ETC devices require surface heat transfer modes to be modelled at all operating temperatures for an accurate description of the device behaviour. An example is the *thermal expansion device* (TED) of Cragun and Howell [7]. A schematic diagram of the

TED and the dimensions of the TED used for the simulations in this example are shown in figure 2(a) and table 2.

Figure 2 shows that both the quantitative and the qualitative nature of behaviour is modelled inaccurately over the *entire* range (300–1500 K) if the effects of radiation and convection are ignored. The very high temperatures (see figure 2(e)) that result from ignoring radiative and convective heat loss from the surface are physically unrealistic and yield downward deflection of the wide arm in figure 2(b). In contrast, the model that includes radiative and convective heat loss yields

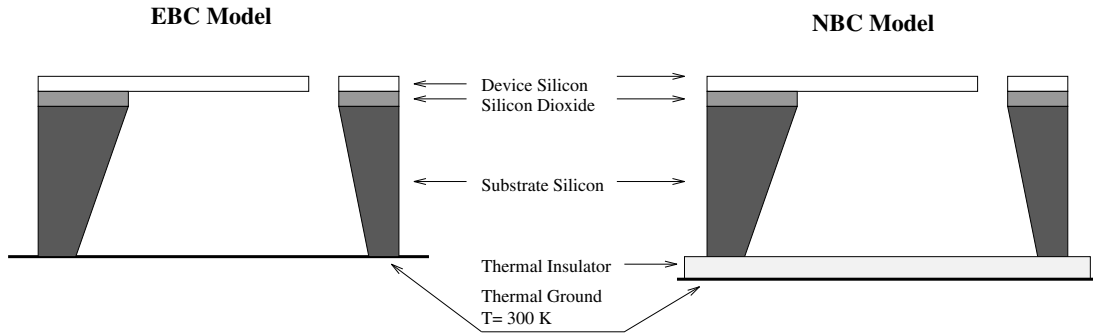


Figure 3. Schematic diagram of the EBC (left) and NBC (right) thermal models.

Table 2. Dimensions of device D1 used for simulations in section 2 (shown in figure 2(a)).

| Dimension | Value (μm) |
|------------------|-------------------------|
| d1 | 40 |
| d2 | 20 |
| d3 | 340 |
| d4 | 100 |
| d5 | 1800 |
| d6 | 40 |
| d7 | 300 |
| d8 | 100 |
| d9 | 1000 |
| d10 | 900 |
| d11 ^a | 20 |

^a Out-of-plane thickness.

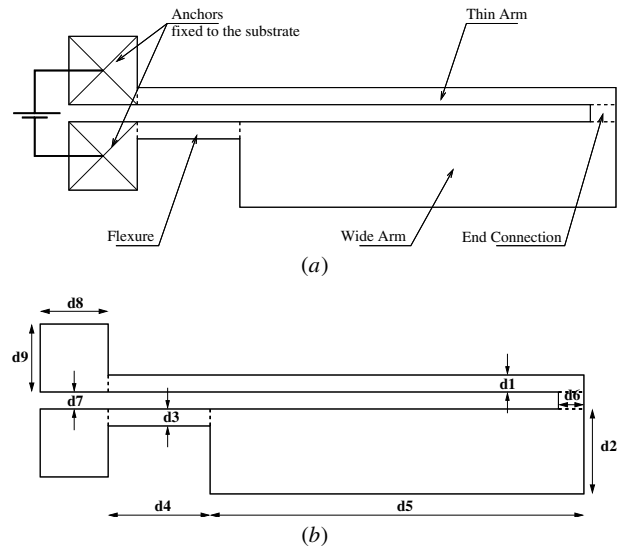


Figure 4. (a) The basic electro-thermal-compliant microactuator (devices D2, D3 and D4) and its dimensioned sketch (b).

an upward deflection of the wide arm as seen in figure 2(c). This is consistent with experimental results for the same range of applied voltage. The thermophysical properties used for the simulations in this example are given in section 3.

This example shows that surface heat transfer by convection is important for modelling the thermal behaviour of a device accurately. Surface heat transfer adds to the complexity of the thermal model because the heat transfer coefficients for a surface are functions of the physical size, shape, orientation and surface condition as well as its temperature.

2.2. Thermal boundary conditions at the anchors

The device is anchored to the substrate at a few places called the *device anchors* which provide mechanical support as well as electrical and thermal connections to the substrate. Thermal models of MEMS devices presented in [8, 11, 22, 24] and others, impose ambient temperature thermal boundary conditions at the device anchors. This choice of thermal boundary condition, referred to as the essential thermal boundary condition (EBC), is justified when the substrate is *thermally grounded* by contact with a large thermal mass at the ambient temperature. However, for devices that do not have access to ideal heat sinking (for example due to the device packaging) the EBC model is inappropriate. Such devices can be modelled by imposing natural or mixed thermal boundary conditions (NBC) at the device anchors. The NBC model restricts heat loss to the substrate and thus improves the energy efficiency of the device significantly. The EBC and NBC models are shown schematically in figure 3. The difference in the behaviour

of the ETC microactuator, when the EBC and NBC models are used, can be seen from the results of the simulations in section 4.

3. Modelling of the basic ETC microactuator

The basic ETC microactuator (figure 4) is used to illustrate the comprehensive thermal modelling described in this paper as a representative of a generic ETC device. The body of the actuator is demarcated into simple geometric shapes as shown in figure 4 for the purpose of modelling. Continuum elements are used in the analysis to model the surface heat loss from all exposed faces of the actuator and also to account for out-of-plane elastic deformations and possible buckling conditions.

For a dc excitation of the domain, the rate of thermoelastic deformation is small. Hence the elastic boundary value problem can be solved after the steady-state temperature field has been obtained from the fully coupled electro-thermal analysis. ABAQUS enables the modelling of temperature dependence of thermophysical properties such as electrical and thermal conductivity, film coefficients, the coefficient of linear thermal expansion and Young’s modulus, by setting up a look-up table of property values and corresponding

temperatures. The NBC thermal model is implemented by specifying an ‘overall’ heat transfer coefficient h_a for the bottom face of the device anchor. This approach is computationally more efficient than having to mesh the substrate of the device. The coefficient h_a can be obtained in a simple manner from a one-dimensional analysis of heat conduction from the anchors to the ground. A more accurate estimate of the overall heat transfer coefficient can be obtained from separate three-dimensional FE simulations that involve meshing of the substrate. Intra-device radiation and conduction can be modelled in ABAQUS by defining a pair of interacting (master/slave) surfaces that participate in the heat exchange. This heat exchange can be modelled to depend not only on temperature but also the inter-surface spacing for nonlinear analysis. A ‘conductive heat transfer coefficient’ can be added to the natural convection coefficient for the bottom face of the device to simulate heat transfer by conduction from the lower face of the device to the substrate. The conductive heat transfer coefficient will include thermal resistance of the intervening air film and surface resistances of the two surfaces concerned.

There is a limited amount of published data on natural convection correlations for heated horizontal plates, suspended over shallow semi-enclosed cavities, losing heat from all exposed surfaces. Jonsmann *et al* [12] have used experimentally determined overall film coefficients while Sigmund [25] has approximated the correlations for a heated horizontal cylinder of suitable diameter in place of those for a plate. In this paper, the plate is modelled as a heated horizontal plate that is convecting heat from all exposed faces. This approximation was observed to yield better agreement with experimental data than the horizontal cylinder approximation due to marked differences in the pattern of air flow around the two bodies. The convective heat loss (film) coefficient is determined independently for each exposed face of every segment of the actuator. The film coefficient for the upper face of a segment is obtained as the natural convection coefficient for heat loss from a hot horizontal plate, of the same dimensions, facing upwards. The film coefficients for the bottom face and edges of each segment are obtained in a similar manner. The expressions for these film coefficients are given in Mills [21]. The range of validity of published data does not cover the entire Rayleigh number range of interest in the context of ETC devices fabricated from mono-crystalline silicon. Hence, wherever necessary, data have been obtained by extrapolation. Although this is an approximation, it serves as a good starting point for the modelling endeavour. All heat radiating surfaces are modelled as grey bodies with an emissivity of 0.7. The conductive heat transfer from the bottom face of the device to the substrate via trapped air volumes has not been used for the simulations of the microactuator in this paper because the devices studied here are separated from the substrate by thick (450 μm) air films.

The doping profile varies from one device to another on a wafer because of process variations. This makes it difficult to determine one value of resistivity that can be used in the simulation of the entire device. It is, however, straightforward to determine the overall device resistance for each value of the applied voltage. If we assume a uniform doping profile for the fabricated devices, then with the knowledge of device

Table 3. Dimensions for the devices D2, D3 and D4.

| Description | Value (μm) | | |
|-------------|-------------------------|-----------|-----------|
| | Device D2 | Device D3 | Device D4 |
| d1 | 40 | 150 | 4 |
| d2 | 255 | 1150 | 25.5 |
| d3 | 40 | 150 | 4 |
| d4 | 330 | 1000 | 33 |
| d5 | 1900 | 2500 | 190 |
| d6 | 90 | 200 | 9 |
| d7 | 75 | 200 | 7.5 |
| d8 | 352 | 2000 | 35 |
| d9 | 352 | 2000 | 35 |
| d11a | 20 | 50 | 2 |

^a Out-of-plane thickness.

Table 4. Thermophysical properties used in the simulation.

| Description | Value |
|--|----------------------|
| Young’s modulus, E (GPa) | 169.0 |
| Poisson ratio, ν | 0.3 |
| Coefficient linear thermal expansion, α | (see table 5) |
| Thermal conductivity, k_t | (see table 5) |
| Electrical resistivity ^a , $1/k_e$ | (see table 6) |
| Emissivity, ϵ | 0.7 |
| Film heat transfer coefficient | (see tables 7 and 8) |

^a Reference value is $4.2 \times 10^{-4} \Omega \text{ m}$ at 300 K.

geometry we can obtain an *effective* resistivity for the entire device at that level of applied voltage. The dependence of measured device resistance on applied voltage is used in place of the temperature dependence of resistivity in the validation process.

The model is validated by comparison with experimental results for both the EBC and NBC thermal boundary condition models. The validation results are shown in figure 5 for both, the EBC model (device D2), which was fabricated by the in-house PennSOIL [2] bulk micromachining process and the NBC model (device D3), which was micromachined by a KrF excimer laser [26]. The two processes have different critical dimension capabilities. This is reflected in the dimensions for the two devices shown in table 3.

The error bars for the EBC model correspond to an uncertainty in measurement of $\pm 8.5 \mu\text{m}$. The measurement for the NBC model was done by a more accurate and recently acquired instrument and consequently has an uncertainty of $\pm 1 \mu\text{m}$.

The thermophysical properties and their variation with temperature for doped single-crystal silicon used for the simulation are summarized in tables 4–8.

4. Simulations

The comprehensive model of the basic ETC actuator was used to study the influence of thermal boundary conditions at the device anchor and size on the steady-state performance of the microactuator. Current manufacturing technology enables the fabrication of the microactuator at different physical scales. Devices with a footprint of 1 mm^2 or less are called *micro scale* devices, while devices with a footprint of $1\text{--}10 \text{ mm}^2$ are called *meso scale* devices in this paper. It is possible to

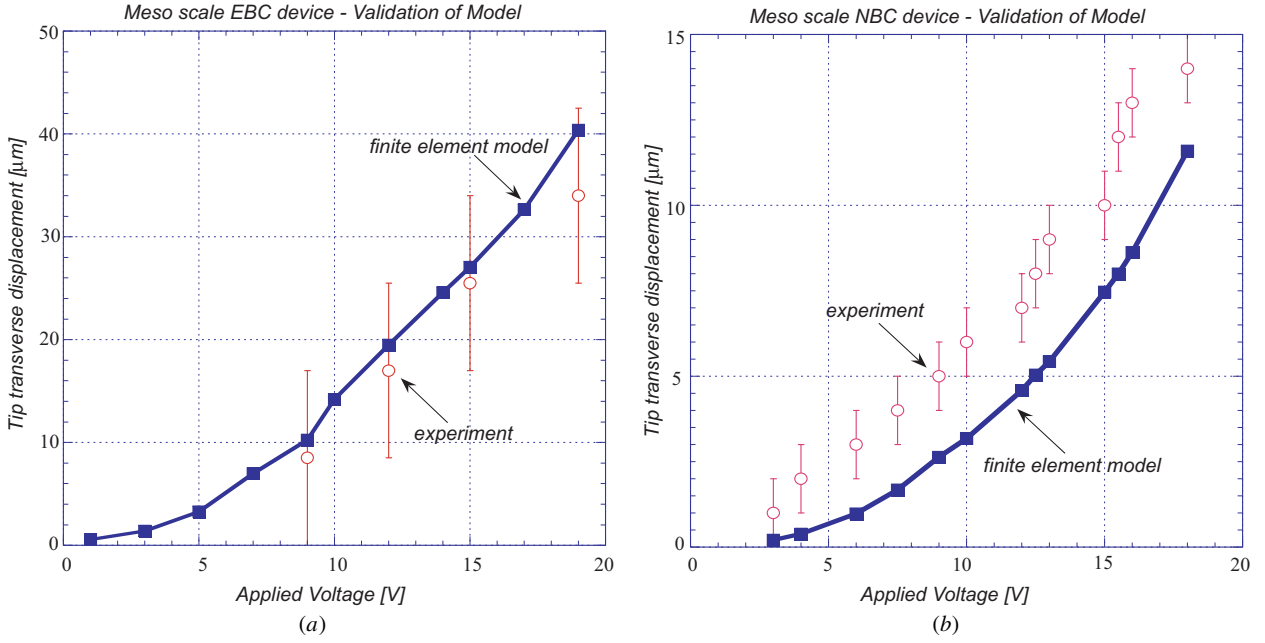


Figure 5. Model validation against experimental data: (a) tip transverse deflection for EBC model microactuator (device D2); and (b) tip transverse deflection for NBC model microactuator (device D3).

Table 5. Variation of coefficient of linear thermal expansion α [19] and thermal conductivity k_t [16] with temperature.

| α ($\mu\text{m m}^{-1} \text{K}^{-1}$) | k_t ($\text{W m}^{-1} \text{K}^{-1}$) | Temperature (K) |
|---|---|-----------------|
| 2.568 | 146.4 | 300 |
| 3.212 | 98.3 | 400 |
| 3.594 | 73.2 | 500 |
| 3.831 | 57.5 | 600 |
| 3.987 | 49.2 | 700 |
| 4.099 | 41.8 | 800 |
| 4.185 | 37.6 | 900 |
| 4.258 | 34.5 | 1000 |
| 4.323 | 31.4 | 1100 |
| 4.384 | 28.2 | 1200 |
| 4.442 | 27.2 | 1300 |
| 4.500 | 26.1 | 1400 |
| 4.556 | 25.1 | 1500 |

Table 6. Experimentally determined variation of device resistance with applied voltage for device D2 and device D3.

| Voltage (V) | Device resistance (Ω) | |
|-------------|--------------------------------|-----------|
| | Device D2 | Device D3 |
| 1 | 1575 | 424.6 |
| 3 | 1304 | 433.5 |
| 5 | 1152 | 441.0 |
| 8 | 1124 | 467.8 |
| 10 | 1149 | 496.8 |
| 12 | 1200 | 535.7 |
| 14 | 1261 | 577.1 |
| 16 | 1356 | 613.0 |
| 18 | 1406 | 632.7 |

control the nature of thermal boundary conditions at the device anchor by choosing an appropriate mounting for the device. In light of this, the motivation for this study was to establish a basis for selection of device size and the type of thermal

boundary condition (EBC or NBC) when designing a basic actuator for a given application. The following configurations were simulated:

- EBC thermal model for a meso scale device;
- NBC thermal model for a meso scale device;
- EBC thermal model for a micro scale device;
- NBC thermal model for a micro scale device.

The meso scale device (see table 3 for device D2) used for the simulation has a footprint of approximately 1 mm^2 ($L \times W \times T = 2230 \times 365 \times 20 \mu\text{m}$), while the micro scale device (see table 3 for device D4) is a 1:10 reduction ($L \times W \times T = 223 \times 36.5 \times 2 \mu\text{m}$) of the meso scale device.

A constant value of $4.2 \times 10^{-4} \Omega \text{ m}$ is used for electrical resistivity in the simulations in this section. Standardized values for variation of the Young’s modulus of single-crystal silicon with temperature have only become available recently [18] and have not been accounted for in the simulations. The rest of the thermophysical properties used in the simulation for the meso scale device are as given in tables 4, 5 and 7, while those used for the micro scale device are summarized in tables 4, 5 and 9.

The deflection of the actuator tip, perpendicular to its length, and the output force corresponding to that displacement, are the outputs of interest. The tip deflection is normalized with respect to the overall device length to eliminate the bias of size. The difference in the average temperatures of the thin and wide arms is a measure of the *non-uniformity* of heating. The output force and deflection depend on the stiffnesses of the load and the actuator. However, the *no load* tip deflection is independent of the load. Similarly, the strain energy stored in the actuator at no load, is a measure of work output, which is independent of the load. A normalized performance ratio is defined for the actuator, as $\eta = SE \cdot \mathcal{N}/P_{in}$; where SE is the strain energy stored in the actuator (excluding the anchors), \mathcal{N} is a normalization

Table 7. Variation of convective heat transfer coefficients ($\text{W m}^{-2} \text{K}^{-1}$) [21] with temperature for model of device D2.

| Temperature (K) | Thin arm and flexure | | Wide arm | | End connection | | Anchor ^a | Side wall |
|-----------------|----------------------|-----------|----------|-----------|----------------|-----------|---------------------|-----------|
| | face up | face down | face up | face down | face up | face down | | |
| 301 | 17.8 | 22.4 | 11.2 | 13.0 | 15.0 | 24.0 | 10.3 | 929 |
| 500 | 60.0 | 69.3 | 37.9 | 39.6 | 50.9 | 73.8 | 35.0 | 1193 |
| 700 | 65.6 | 76.1 | 41.4 | 43.6 | 55.5 | 81.0 | 38.2 | 1397 |
| 900 | 68.9 | 80.5 | 43.4 | 46.0 | 58.2 | 85.7 | 40.0 | 1597 |
| 1100 | 71.1 | 83.7 | 44.8 | 47.6 | 60.0 | 89.2 | 41.3 | 1791 |
| 1300 | 72.6 | 86.0 | 45.7 | 49.0 | 61.2 | 91.6 | 42.1 | 1982 |
| 1500 | 73.2 | 87.5 | 46.0 | 50.1 | 62.7 | 93.2 | 42.5 | 2176 |

^a 240.0 for lower face in NBC model of D2 corresponding to $0.1 \mu\text{m}$ oxide + $430 \mu\text{m}$ substrate + $2 \times 2 \text{ mm}$ Kodak plate glass.

Table 8. Variation of convective heat transfer coefficients ($\text{W m}^{-2} \text{K}^{-1}$) [21] with temperature for model of device D3.

| Temperature (K) | Thin arm and flexure | | Wide arm | | End connection | | Anchor ^a | Side wall |
|-----------------|----------------------|-----------|----------|-----------|----------------|-----------|---------------------|-----------|
| | face up | face down | face up | face down | face up | face down | | |
| 301 | 12.8 | 14.8 | 7.7 | 8.9 | 12.0 | 18.4 | 6.7 | 379.5 |
| 500 | 43.3 | 45.7 | 23.0 | 27.2 | 40.3 | 56.6 | 8.0 | 504.3 |
| 700 | 47.2 | 50.2 | 25.1 | 29.9 | 44.0 | 62.2 | 8.5 | 588.1 |
| 900 | 49.5 | 53.1 | 26.8 | 31.6 | 46.1 | 65.8 | 8.6 | 669.8 |
| 1100 | 51.1 | 55.3 | 29.2 | 32.9 | 47.6 | 68.4 | 8.7 | 748.0 |
| 1300 | 52.1 | 56.8 | 30.8 | 33.9 | 48.5 | 70.3 | 8.6 | 825.5 |
| 1500 | 52.6 | 57.8 | 31.6 | 34.5 | 49.0 | 71.6 | 8.4 | 903.5 |

^a 461.0 for lower face in NBC model of D3 corresponding to $100 \mu\text{m}$ Omega CC high-temperature cement + 2 mm Kodak plate glass.

Table 9. Variation of convective heat transfer coefficients ($\text{W m}^{-2} \text{K}^{-1}$) [21] with temperature for model of device D4.

| Temperature (K) | Thin arm and flexure | | Wide arm | | End connection | | Anchor ^a | Side wall |
|-----------------|----------------------|-----------|----------|-----------|----------------|-----------|---------------------|-----------|
| | face up | face down | face up | face down | face up | face down | | |
| 301 | 31.6 | 49.4 | 19.9 | 27.0 | 26.6 | 49.4 | 18.3 | 9 120.0 |
| 500 | 107.2 | 153.2 | 67.5 | 83.5 | 90.5 | 153.2 | 62.2 | 11 370.0 |
| 700 | 116.9 | 168.2 | 73.6 | 91.7 | 98.7 | 168.2 | 67.9 | 13 360.0 |
| 900 | 122.6 | 177.8 | 77.2 | 97.0 | 103.4 | 177.8 | 71.2 | 15 340.0 |
| 1100 | 126.4 | 184.9 | 79.6 | 100.8 | 106.7 | 184.9 | 73.4 | 17 240.0 |
| 1300 | 128.9 | 190.0 | 81.2 | 103.7 | 108.8 | 190.0 | 74.9 | 19 150.0 |
| 1500 | 130.1 | 193.3 | 81.9 | 105.4 | 109.8 | 193.3 | 75.5 | 198 970.0 |

^a 240.0 for lower face in NBC model of D4 corresponding to $0.1 \mu\text{m}$ oxide + $430 \mu\text{m}$ substrate + $2 \times 2 \text{ mm}$ Kodak plate glass.

factor and P_m is the electrical power input. The reciprocal of the highest performance ratio over all devices and applied voltages is chosen as \mathcal{N} . The results of the simulations are summarized in figures 6, 7, 8 and 9 that can be thought of as the *no load operating characteristics* of the microactuator.

5. Observations and discussion

5.1. Observations

Figure 6 shows that the normalized tip deflection is independent of the size for a given type of thermal model. The NBC model yields a consistently higher normalized transverse tip deflection (stroke) than the EBC model. On average, the NBC model yields a 66.5% improvement in the stroke of the microactuator for the same applied voltage at both scales. The axial or lengthwise displacement of the actuator, due to unconstrained thermal expansion, is a parasitic effect that causes buckling in opposed arrays of microactuators. Figure 6

also shows that the normalized axial displacement follows the same trend as the normalized transverse displacement but is approximately an order of magnitude smaller than the transverse displacement for both thermal boundary conditions and physical sizes. The normalized performance ratio increased by approximately two orders of magnitude when the characteristic length of the microactuator was increased by one order of magnitude from 0.22 mm to 2.2 mm , as shown in figure 7. The NBC model devices have a consistently higher performance ratio than the EBC model devices at both scales. Thus, on average, a NBC model device is four times as efficient as the corresponding EBC device at both scales over the temperature range $300\text{--}1500 \text{ K}$. An important observation, summarized in figure 8, is the linear dependence of the normalized transverse and axial displacements on the difference between the average thin and wide arm temperatures. These results do not include the effect of the temperature dependence of resistivity for the reasons discussed in section 4.

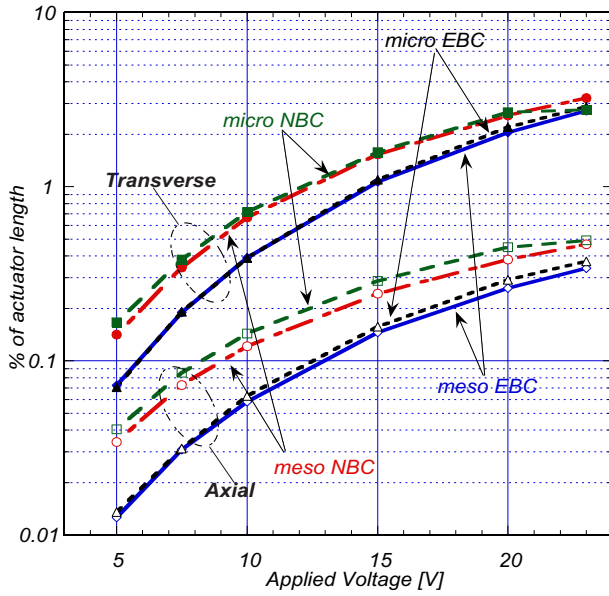


Figure 6. Normalized transverse and axial tip deflection at no load.

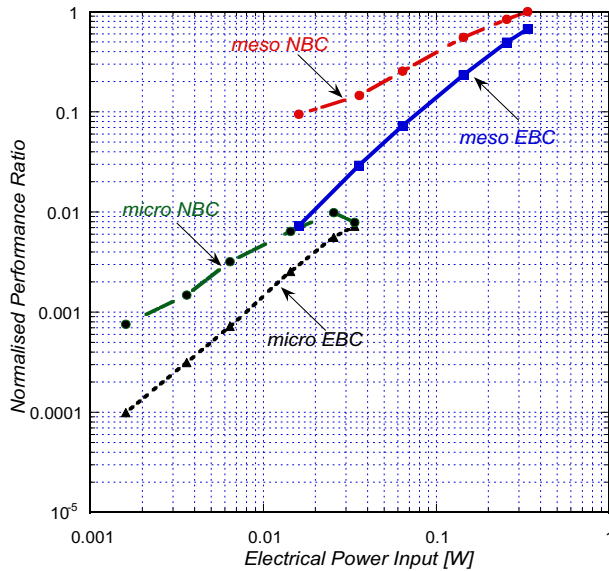


Figure 7. Normalized performance ratio as a function of electrical power input.

5.2. Discussion

The electrical conductivity of silicon can vary within several orders of magnitude depending on the doping level. Furthermore, the nature of temperature dependence of electrical conductivity (i.e. whether electrical conductivity rises or falls with an increase in temperature) is also dependent on the doping level. The doping level thus constitutes an important but widely variable quantity. A constant value of electrical conductivity was chosen for the simulations to eliminate the dependence of the results on specific physical prototypes.

In the absence of temperature dependence of electrical conductivity, the heat generation rate is the same for the EBC and NBC models at the same scale and for the same applied voltage. The EBC model devices conduct a large part of the

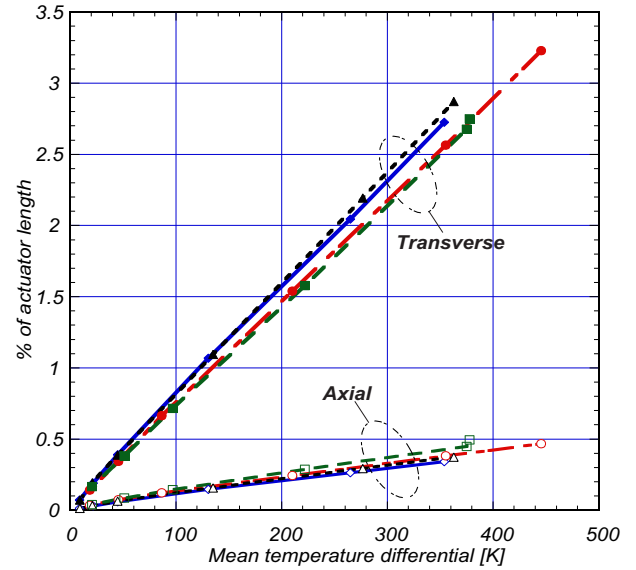


Figure 8. Normalized transverse and axial tip deflection as a function of the non-uniformity of heating.

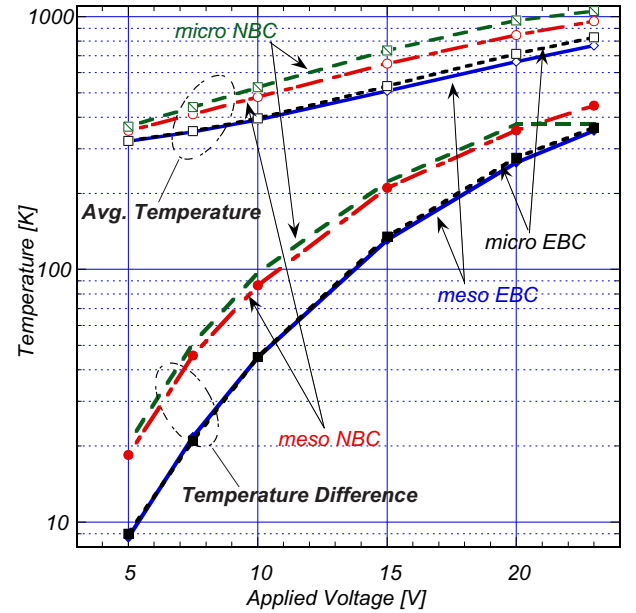


Figure 9. Average temperature for the entire device and difference in the mean thin and wide arm temperatures (i.e. non-uniformity of heating).

electrical input power to the substrate via the anchors. Also, the thermal conductivity of single-crystal silicon decreases rapidly with temperature [17]. The EBC model, therefore, has lower overall temperatures than the corresponding NBC model for the same applied voltage as shown in figure 9. The NBC model has a greater difference in the average thin and wide arm temperatures than the corresponding EBC model at the same applied voltage, for the same reason (see figure 9). Together with the linear dependence of normalized transverse and axial displacements on the difference in the average thin and wide arm temperatures, this results in a higher normalized transverse and axial displacements for the NBC model devices than the EBC model devices at the same applied voltage.

The smaller devices have a higher resistance and a higher current density than the larger devices, for the same power input. This results in a higher internal heat generation for the smaller devices as compared to the larger devices. The smaller devices also lose heat more readily than the larger devices because the film coefficients increase as the size decreases. But they still run at higher overall temperatures than the larger devices because the increase in internal heat generation rate overshadows the increase in surface heat loss as temperature increases (see figure 9). The smaller devices dissipate more heat and hence are less energy efficient as seen in figure 7. In spite of higher overall temperatures, the NBC model devices are more efficient than the EBC model devices because they lose less heat to the substrate via the anchors, which is the dominant mode of heat loss.

These observations motivate the following selection criteria for the microactuator operating under steady-state (static) conditions:

- The scale of the actuator is chosen to be consistent with the stroke required keeping in mind that performance ratio degrades sharply with a decrease in size. It should also be borne in mind that a decrease in size results in an increase in the overall temperature of operation.
- The NBC model can be chosen for a higher performance ratio if the corresponding higher operating temperatures are acceptable. In particular, the NBC model can be used to improve the poor performance ratio when a small device size is necessary.

6. Conclusion

A comprehensive thermal modelling paradigm for simulation and analysis of generic ETC devices over a wide range of maximum operating temperatures (300–1500 K) has been presented using the basic ETC microactuator as an example. The comprehensive model is independent of the device being tested and uses standard material/process-dependent properties from a process-oriented material property database. The model for the microactuator was validated by experiments and was used for the *virtual testing* of the microactuator over a wide temperature range.

The comprehensive model was used to investigate the effect of thermal boundary conditions at device anchors and physical size on the behaviour of a family of geometrically similar ETC microactuators. The temperature dependence of electrical conductivity was not included in the investigation. It was observed that the transverse displacement (stroke) of the microactuator was proportional to the overall length of the device. The performance ratio for the microactuator increased by a factor of a hundred when the characteristic length of the device was increased by a factor of ten. The smaller devices had higher overall temperatures. The NBC thermal model, which restricts heat loss by conduction to the substrate via the device anchors, yielded an average improvement in stroke of 66% over the conventional EBC thermal model. The NBC model also improved the performance ratio of the microactuator by a factor of four as compared to the EBC model.

The investigation, thus, showed that device size was a primary determinant of stroke, operating temperature and

performance ratio for the microactuator. The thermal boundary conditions at the device anchors also control the stroke, operating temperature and performance ratio of the microactuator and can be manipulated in conjunction with the device size to obtain an optimal ETC microactuator design for a given application.

Acknowledgments

This research is supported by The National Science Foundation through the grant DMI-97-33196 CAREER. The authors would like to thank Timothy Moulton for valuable discussions and Jun Li for help with fabrication and testing the ETC devices used to validate the model presented in this work.

References

- [1] Reithmüller W and Benecke W 1988 Thermally excited silicon microactuators *IEEE Trans. Electron Devices* **35** 758–62
- [2] Moulton T and Ananthasuresh G K 2001 Micromechanical devices with embedded electro-thermal-compliant actuation *Sensors Actuators A* **90** 34–48
- [3] Guckel H, Klein J, Christenson T, Skrobis K, Laudon M and Lovell E G 1992 Thermo-magnetic metal flexure actuators *Technical Digest, 1992 Solid-State Sensors and Actuators Workshop (Hilton Head, SC, USA)* pp 73–5
- [4] Que L, Park J S and Gianchandani Y B 1999 Bent beam electro-thermal actuators for high force applications *Proc. MEMS'99* pp 31–6
- [5] Comtois J H, Michalick M A and Barron C G 1998 Electrothermal actuators fabricated in four-level planarized surface micromachined polycrystalline silicon *Sensors Actuators A* **70** 23–31
- [6] Comtois J and Bright V 1996 Surface micromachined polysilicon thermal actuator arrays and applications *Proc. Solid-State Sensors and Actuators Workshop (Hilton Head, SC, USA)* pp 174–7
- [7] Cragun R and Howell L H 1998 A constrained thermal expansion microactuator *Micro-Electro-Mechanical systems (MEMS), ASME DSC-66* 365–71
- [8] Huang Q-A and Lee N K 1999 Analysis and design of polysilicon thermal flexure actuator *J. Micromech. Microeng.* **9** 64–70
- [9] Reid J R, Bright V M and Comtois J H 1996 Force measurements of polysilicon thermal microactuators *Micromachined Devices and Components II* **2882** 296–306
- [10] Lerch P, Slimane C K, Romanowicz B and Renaud P 1996 Modelization and characterization of asymmetrical thermal microactuators *J. Micromech. Microeng.* **6** 134–7
- [11] Lin L and Chiao M 1996 Electrothermal responses of lineshape microstructures *Sensors Actuators A* **55** 35–41
- [12] Jonsmann J, Sigmund O and Bouwstra S 1999 Compliant electro-thermal microactuators *Proc. MEMS'99* pp 588–93
- [13] Polder D and Hove M V 1971 Theory of radiative heat transfer between closely spaced bodies *Phys. Rev. B* **4** 3303–14
- [14] Pan C S and Hsu W 1997 An electro-thermally and laterally driven polysilicon microactuator *J. Micromech. Microeng.* **7** 7–13
- [15] Lin L and Lin S-H 1998 Vertically driven microactuators by electrothermal buckling effects *Sensors Actuators A* **71** 35–9
- [16] Lide D R and Kehiaian H V (eds) 1994 *CRC Handbook of Thermophysical and Thermomechanical Data* (Ann Arbor, MI: CRC Press)
- [17] Touloukian Y S (ed) 1967 *Thermophysical Properties of High Temperature Solid Materials: Elements* vol I (New York: Macmillan)

- [18] Ono N, Kitamura K, Nakajima K and Shimanuki Y 2000 Measurement of Young's modulus of silicon single crystal at high temperature and its dependency on boron concentration using the flexural vibration method *Japan. J. Appl. Phys.* **39** A368–71
- [19] Okada Y and Tokumaru Y 1984 Precise determination of lattice parameter and thermal expansion coefficient of silicon between 300 and 1500 K *J. Appl. Phys.* **56** 314–20
- [20] Mankame N D and Ananthasuresh G K 2000 Effect of thermal boundary conditions and scale on the behaviour of electro-thermal-compliant micromechanisms *Proc. of Modeling and Simulation of Microsystems MSM2000 (San Diego, CA, 2000)* pp 609–12
- [21] Mills A F 1999 *Basic Heat and Mass Transfer* (Upper Saddle River, NJ: Prentice Hall)
- [22] Mastrangelo C H, Yeh J H-J and Muller R S 1992 Electrical and optical characteristics of vacuum sealed polysilicon microlamps *IEEE Trans. Electron Devices* **39** 1363–74
- [23] Hibbitt, Karlsson and Sorensen, Inc 1998 *ABAQUS/Standard* version 5.8
- [24] Lin L and Pisano A P 1991 Bubble forming on a micro line heater *Micromechanical Sensors, Actuators and Systems, ASME DSC-32* 147–63
- [25] Sigmund O 1998 Topology optimization in multiphysics problems *Proc. 7th AIAA/USAF/NASA/ISSMO Symp. (St Louis)* vol 3, pp 1492–500
- [26] Li J and Ananthasuresh G K 2001 A quality study on the excimer laser micromachining of electro-thermal-compliant microdevices *J. Micromech. Microeng.* **11** 38–47